Sky and Elemental Planetary Mapping via Gamma Ray Emissions

John M. Roland[1]
Jet Propulsion Laboratory, California Institute of Technology, Pasadena, CA 91109

Mentors: Dr. James Ling[2] and Dr. Martin Lo[3]
Jet Propulsion Laboratory, California Institute of Technology, Pasadena, CA 91109

Low-energy gamma ray emissions (~30keV to ~30MeV) are significant to astrophysics because many interesting objects emit their primary energy in this regime. As such, there has been increasing demand for a complete map of the gamma ray sky, but many experiments to do so have encountered obstacles. Using an innovative method of applying the Radon Transform to data from BATSE (the Burst And Transient Source Experiment) on NASA's CGRO (Compton Gamma-Ray Observatory) mission, we have circumvented many of these issues and successfully localized many known sources to 0.5 - 1° accuracy. Our method, which is based on a simple 2-dimensional planar back-projection approximation of the inverse Radon transform (familiar from medical CAT-scan technology), can thus be used to image the entire sky and locate new gamma ray sources, specifically in energy bands between 200keV and 2MeV which have not been well surveyed to date. Samples of these results will be presented. This same technique can also be applied to elemental planetary surface mapping via gamma ray spectroscopy. Due to our method's simplicity and power, it could potentially improve a current map's resolution by a significant factor.

I. Introduction to Sky Mapping

Historically, the low energy gamma ray sky from ~30keV to ~30MeV has not been well documented. Due to the low photon source fluxes (which generally decrease with energy like E^{-2} or faster) and the high penetrating nature of gamma rays over 100keV, successfully locating gamma ray sources using a standard collimated detector has its limitations. However, as these electromagnetic waves are so penetrating, they are able to carry a great deal of information about heavily obscured sources, which are unobservable in any other spectrum. These sources can be some of the most interesting objects in high-energy astrophysics including super-massive black holes that power the central engines of Active Galactic Nuclei, neutron stars and supernova remnants such as the Crab,[21] outbursts of luminous galactic gamma-ray transients, e.g. GRO J1719-24[23] and GRO J0422+32,[22] and stellar-mass black holes like Cygnus X-1.[19] As such, mapping the gamma ray sky is a priority of the astrophysics community.

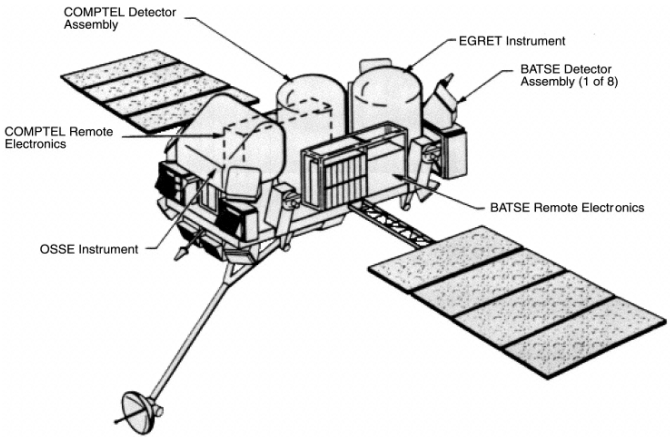

Figure 1. *A diagram of CGRO showing the four experiments aboard. Notice that BATSE has eight detectors in the corners of the satellite.*

The BATSE experiment on NASA's CGRO was designed to measure gamma ray bursts in the universe. It can also be used to image the gamma-ray sky[24] and monitor the long term temporal and spectral characteristics of galactic and extragalactic sources using the earth occultation

[1] Undergraduate Intern from Dartmouth College
[2] Manager, Astrophysics and Heliophysics Research and Analysis Program
[3] Technologist, High Capability Computing and Modeling Group

technique.[20] As can be seen in Fig. 1, the essentially isotropic response of the eight Large Area Detectors on BATSE coupled with the satellite's nine-year exposure time effectively overcomes the low photon source flux issue by continuously gathering a plethora of gamma ray data. Each detector counts the raw number of incident photons every 2.048s and records the data.[30] This wide field of view and massive amount of data, however, cannot successfully locate sources since the detectors are collecting data from multiple directions at any given time.

In order to make use of CGRO's data for gamma ray source location, Dr. Martin Lo and Dr. James Ling's group implemented the Earth occultation technique in conjunction with the Radon Transform tomographic imaging technique to analyze the data. The Earth occultation technique takes advantage of the fact that, while extremely penetrating, gamma rays are blocked by the Earth. Therefore, when a gamma ray source sets (passes behind the Earth), there is a clear drop in gamma ray counts. Similarly, when a source rises (appears from behind the Earth), there is a clear step in counts. As the CGRO revolves around the Earth, its orbit is inclined 29° and, thus, precesses about the Earth's axis with ~51 day period. This precession allows the satellite to "view" the entire gamma ray sky by recording occultation data.

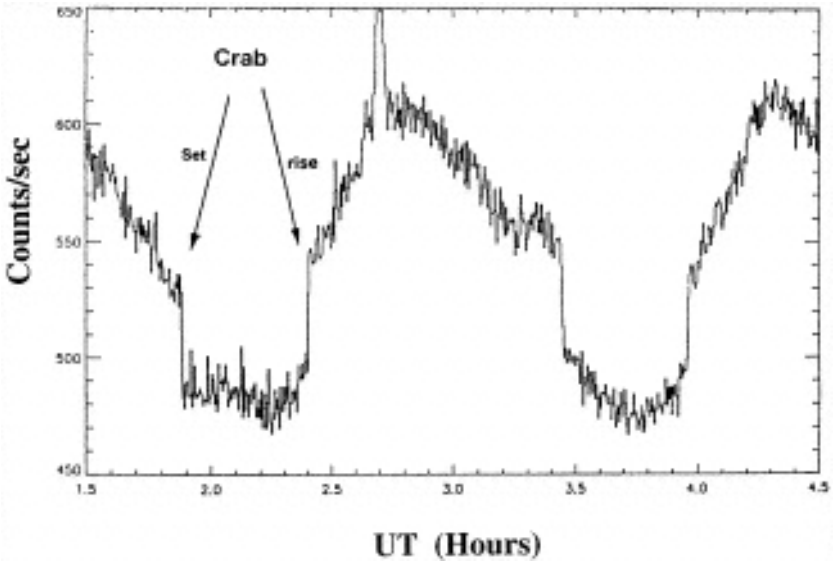

Figure 2. *BATSE count rate data for a few hours. Because it is such a strong gamma ray source, the Crab Nebula has an easily identifiable count step. All sources display a similar jump at characteristic amplitudes.*

Since the amplitudes of each gamma ray count step vary within CGRO's precession period, the Earth occultation method is not enough, so the Radon Transform technique must also be applied. Discovered by John Radon in 1917, the Radon Transform is closely related to the Fourier Transform and is the basis for tomographic methods.[15] Due to its ability to image hidden two- and three-dimensional structures easily, the transform has traditionally been used in X-ray imaging and CAT scans and is also being used more frequently for scientific and engineering problems, such as this. The idea behind the technique is to recreate the shape of an object, X, from the integrals of a particular family of subspaces of X. For the BATSE data, this involves using the line integrals through a given plane to reconstruct an image within that plane, the Linear Radon Transform (although theoretically other subspaces in higher dimensions could be used, Generalized Radon Transform). Figure 3 demonstrates this process on an image. Figure 3a is the original image I(x,y) in the plane S. Figure 3b is the Linear Radon Transform (R) of image I produced by integrating the image over all lines L in S:

$$R(I) = \int_L I(x,y)ds = \rho(\theta,b) \qquad (1)$$

where $L = \{y = \tan\theta \cdot x + b\}$ is a line in S. Therefore, knowing $\rho(\theta,b)$, one can reconstruct the original image with the Inverse Radon Transform R^{-1}. Figure 3c displays the reconstructed image after the Inverse Radon Transform has been performed on $\rho(\theta,b)$. For a small patch of the sky, the Earth's limb can be approximated as a straight line, and the difference in gamma ray counts can be seen as the integral along that along that line for a

particular window in the sky. The changing satellite position due to its orbital precession provides a number of these lines though any given window. Therefore by performing the Inverse Linear Radon Transform on this data, taken from BATSE, one can reconstruct the image of the gamma ray sources and thus locate them.

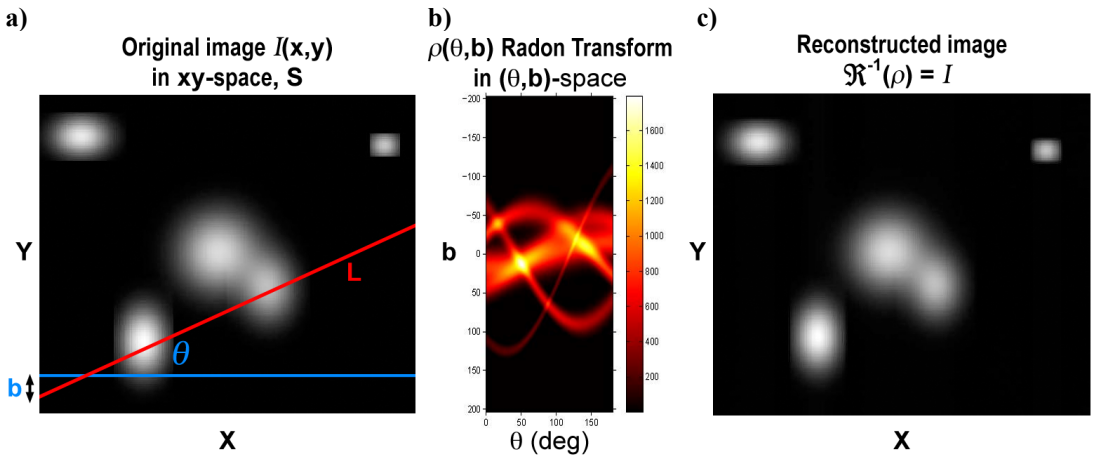

Figure 3. *Idea behind Linear Radon Transform. a) Original image I(x,y) with a family of lines L parameterized by the y-intercept b and the angle with the x-axis θ. b) The image in b-θ space after the Radon Transform has been performed. c) Reconstructed image I after the Inverse Radon Transform has been performed on the image in b-θ space.*

II. Data Analysis

Before the Fall 2009 USRP Session, Lo and Ling's group had begun implementing the Earth Occultation and Inverse Radon Transform techniques in their data analysis with IDL. By building on the Enhanced BATSE Occultation Package (EBOP) data analysis program developed at JPL, they were able to begin locating sources in four broad energy bands (23 - 98 keV, 98 - 230 keV, 230 - 595 keV and 595 -1798 keV) with good accuracy for about 20 known sources.

A. Method

The method for BATSE tomographic mapping of gamma-ray sources consists mainly of 4 parts: 1) creating the raw image of a source, 2) creating the point spread function (PSF), 3) computing the source intensity, and 4) cleaning the image. After choosing a 4˚×4˚ (Right Ascension × Declination) patch to image, the data must first be corrected to account for data gaps, detector efficiencies, and satellite position using algorithms created by Thomas Shimizu (former USRP and SURF intern and current Virtual USRP intern). Using these algorithms, the BATSE count data can be corrected and then inverse radon transformed to produce the raw image of the particular sky patch.

Similarly, the PSF must be corrected and put through the inverse radon transform using simulation data. The PSF is an image created for a point source with the same Inverse Radon Transform technique. It is used to describe the response of an imaging system and can further correct the for the source's position. To produce the PSF, point source data from a given source location are fabricated and then put through the imaging program.

Once the raw image and PSF are created, the intensity can be calculated for a given source and cleaning processes can be applied. To calculate the intensity, the raw image is multiplied by the PSF, pixel by pixel, and then the products are summed. Afterwards, a cleaning process (e.g. Maximum Entropy Method) can be applied to the raw image and PSF to pinpoint the sources location. Lo and Ling's group used these methods in IDL to create corrected images for about twenty strong sources, one of which is shown in Fig. 4.

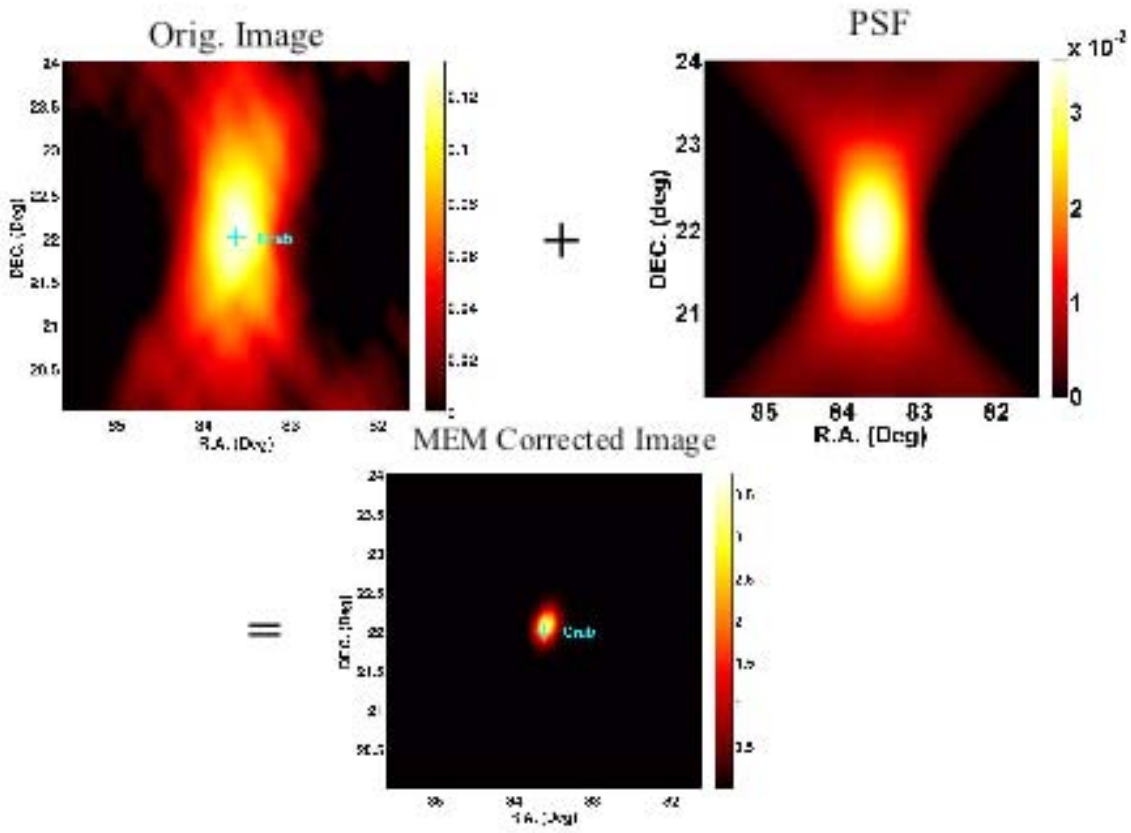

Figure 4. *Diagram of a simplified MEM method on the Crab. The raw image and PSF are input into an MEM program, and after a number of iterations, an image of the Crab to about 0.5˚-1˚ of accuracy is output.*

B. From IDL to Matlab

Despite IDL's high success rate with the initial twenty gamma ray sources, over 135 known sources needed to be imaged next and eventually the entire sky would be processed. Due to licensing issues, IDL was restricted to run on only one processor, so all of the programming needed to be moved from IDL to Matlab. With Matlab, we could make use of our server's parallel processing ability and produce the images in a reasonable amount of time. So Thomas Shimizu and I spent much of our internships making the switch.

After familiarizing myself with Matlab and learning to use the parallel processors, I was able to speed up the raw imaging process by a factor of at least three. I also included code to average the images during and after their creation and code to find consecutive precession periods between two desired imaging dates for transient sources. I made all of this code accessible to the entire group and wrote a user guide so that they could use my imaging programs after the internship had ended.

III. Results

We have completed raw images in all four energy bands for 104 known steady sources over the first twenty precession periods (~51 days) of the BATSE mission and for 35 known transient sources over their burst intervals. For the eighteen images with clear a signal in either energy band three or four (230 - 595 keV and 595 -1798 keV, respectively), we also created images over the remaining forty-four precession periods, giving us images for the full nine years of BATSE data collection. Although these images are not the final step in determining source location, the raw count data give a good indication of position and relative strength within a patch. Many of our raw images have accurately represented the sources' locations, as can be seen in Fig. 5; the green crosses represent the source's known coordinates. One of the most notable features of our technique is its ability to pick up the higher energy signals in bands three and four (e.g. Fig. 5, Crab Nebula, Cygnus X-1, and GRO J0422+32). As one of the few techniques with this capability, the Earth Occultation and Radon Transform method can reveal much of the previously unseen sky.

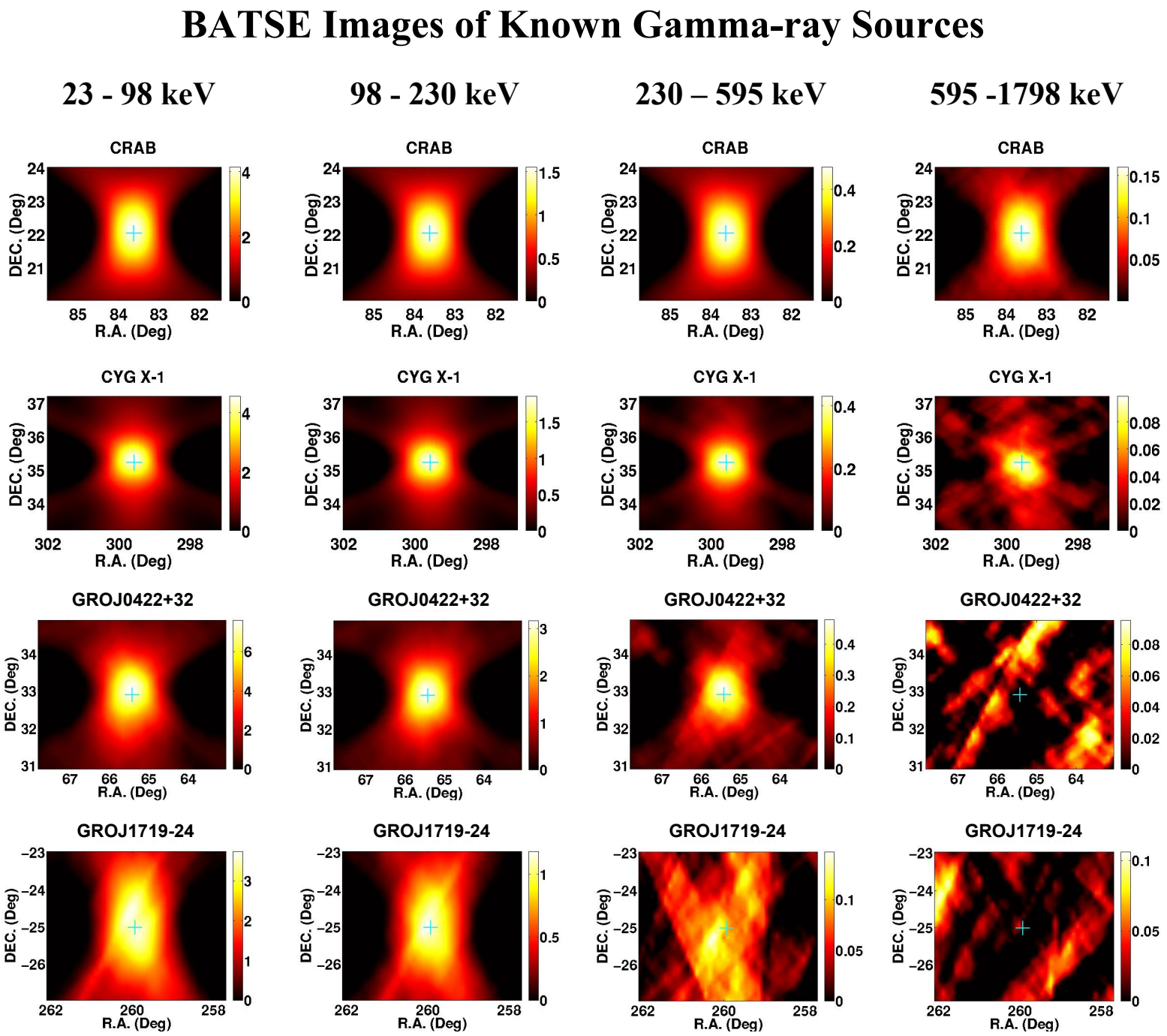

Figure 5. *Raw images of known steady and transient sources in all four energy bands. The first and second rows show image averages of the Crab Nebula and Cygnus X-1, respectively, over the 9-year BATSE mission. The third and fourth rows show GRO J0422+32 and GRO J1719-24 during their respective high state gamma ray bursts (TJD 8841-8891 for GRO J0422+32 and TJD 9262-9312 for GRO J1719-24).*

IV. Project Expansion: Elemental Planetary Mapping

Since gamma-ray emissions play a pivotal role in the elemental mapping of planets and the moon, our method of gamma ray analysis could be applied here and potentially improve elemental concentration maps by a significant factor. Due to radioactive decay or neutron-induced excitations, elements in the regolith emit gamma rays at discrete energy levels. As these energy levels are well documented, gamma ray spectra collected above planets can be used for the identification of elements and their concentrations. NASA already has spacecrafts with gamma ray detectors, e.g. the Gamma Subsystems on the Mars Odyssey[3] and the Lunar Prospector,[2] in orbit around Mars and the moon supplying us with gamma ray data, but the current methods yield a fair amount of uncertainty, particularly in areas of low elevation. Producing more accurate maps will result in more informed Lunar and Martian missions and will expedite planetary exploration. (The following sections detail the Mars Odyssey.)

A. Instrumentation[3]

The Mars Odyssey Gamma-Ray Spectrometer is a suite consisting of three separate instruments: a gamma subsystem (GS), a neutron spectrometer, and a high-energy neutron detector. Within the GS, the gamma ray spectra are actually collected at the Gamma Sensor Head (GSH) at a rate of one per degree (360 spectra per orbit for a duration of about 19.75 s each).[3,4] Each collected spectrum has 16,384 channels of discrete counts (0 to 10 MeV), and since the gamma ray intensities from a planetary surface are so low, each photon is counted individually and sorted by energy.[4] The photon detectors are composed of a large single crystal of n-type ultrahigh-purity Ge with semi-conductor electrodes implanted such that the crystal becomes a diode. When a photon enters, the interaction creates a hole-electron pair, each component of which is swept to the appropriate diode. The small charge is collected by a sensitive preamp that produces a voltage pulse proportional to the energy deposited in the crystal. Like the BATSE Large Area Detectors, these detectors are not collimated, which results in a large satellite footprint (as seen in Fig. 6). The footprint size varies as a function of the production and energy of the gamma ray but generally has a 240 km (4.1˚) radius.[3] (A satellite footprint is defined by 50% of the signal area.)

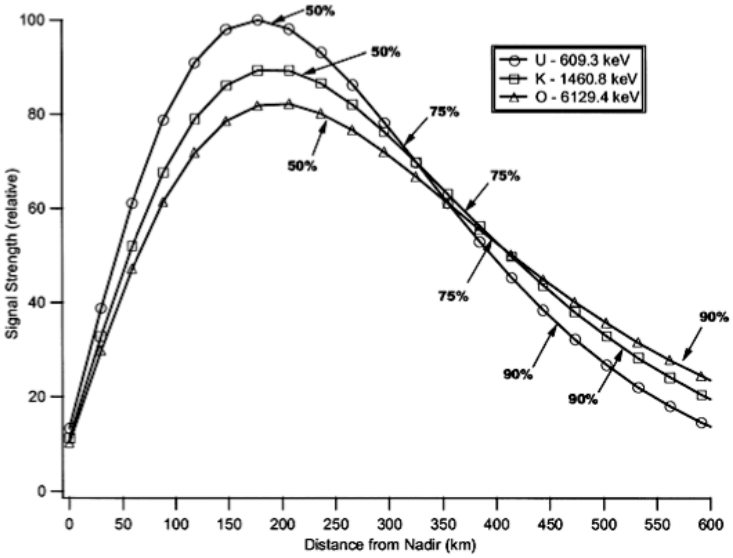

Figure 6. *Signal intensity as a function of distance from the sub-spacecraft point for three gamma-ray energies. The signal initially increases with distance from the nadir because the area of each annulus increases; it then drops off due to the attenuation through a greater path length through the soil and atmosphere.*

The neutron data are useful for determining the excitation flux for the gamma rays made by nuclear reactions. The neutrons are collected at both the neutron spectrometer detector and the high-energy neutron detector. The neutron spectrometer detector is a cubical block of boron-loaded plastic scintillator that is segmented into four optically isolated, prism-shaped quadrants each with a photomultiplier tube (PMT). One quadrant is oriented in the direction of the nadir (N), another in the direction of the zenith (Z), another in the direction of the velocity (+V), and the last one opposite the direction of the velocity (-V). When a neutron enters the spectrometer, it loses energy through multiple elastic scattering collisions with the H and C nuclei that comprise the scintillator. Most of this energy is lost in proton recoils. As the protons slow down, they produce ion-electron pairs which recombine to produce photons. The PMT's collect these photons, and a pulse is produced which is amplified, digitized, and recorded to generate a histogram. If all the neutron energy is deposited in the scintillator, a $^{10}B(n, \alpha)^{7}Li$ reaction occurs, triggering single pulse for thermal (below ~0.1eV) or epithermal (~0.1-100eV) neutrons and time correlated double pulse represents fast (~0.6-8Mev) neutrons.[3] The downward facing prism is covered with a cadmium sheet so that it only responds to epithermal and fast neutrons. Thus, this prism is used to measure the flux of epithermal neutrons. Since Odyssey travels faster than thermal neutrons, the difference between the forward and backward facing prisms provides a

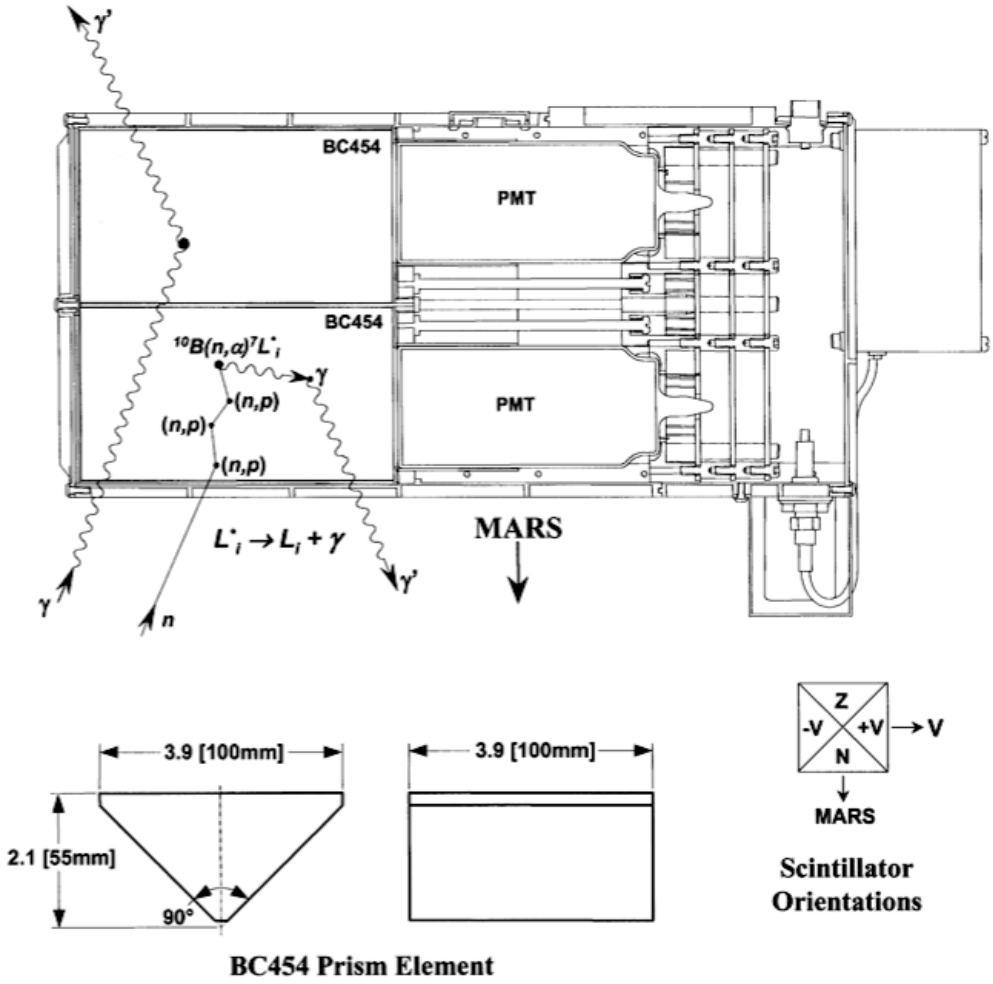

Figure 7. *Drawing of the GRS neutron spectrometer sensor head showing two of the four BC454 prisms in cross section with their associated PMT. The orientation of the prisms and a schematic of the neutron interactions are also shown.*

measure for the flux of the thermal neutrons. The high-energy neutron detector is a set of sensors with three ^{3}He proportional counters. The small Detector is most sensitive at 0.4eV–1keV, the medium detector at 0.4eV–100keV, and the large detector at 10eV–1MeV. The three detectors produce three separate signals (SSD, SMD, SLD) when a neutron interacts with them.

B. Deconvolution of the Signal[14]

The gamma ray detector's wide field of view makes it unclear as to where photons of a given originated, so the signal must be deconvolved. For a given element, the relationship between a map of an elemental distribution on the Martian surface, $M(\theta,\phi)$, and the map of that distribution as measured by an orbiting gamma ray spectrometer, $H(\theta',\phi')$, is described by the convolution integral:

$$H(\theta',\phi') = \int_s R(\cos\varepsilon)\cdot M(\theta,\phi)ds \qquad (2)$$

where $R(\cos\varepsilon)$ is the response function of an isotropic detector and ε is the angle between the position of the emission source on the planet's surface (θ,ϕ) and the orbiter's nadir (θ',ϕ') measured from the planet's center (see Fig. 8). The integration is performed over the spectrometer's entire field of view, S. Equation (2) tells us that

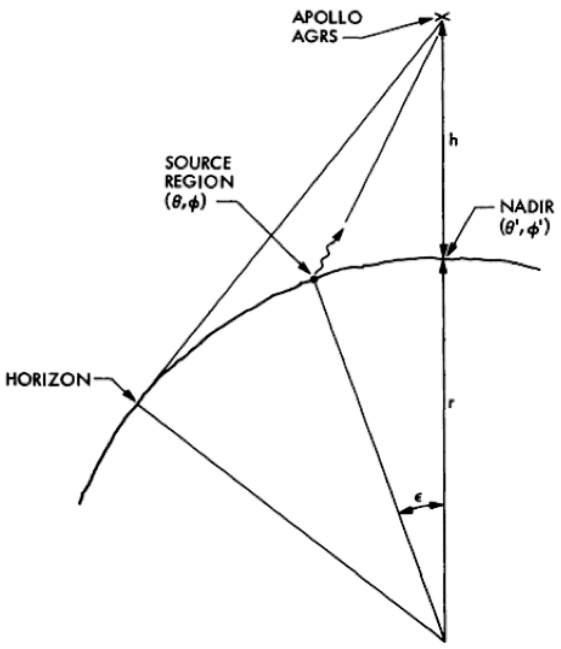

Figure 8. *Geometric representation of the gamma ray's origin in relation to the satellite's position.*

given the response function of the detector and the detailed distribution of the element at the Martian surface we can determine the distribution as mapped by the satellite. Since we have H and want to find M, we must deconvolve the elemental concentration maps.

In order to deconvolve this map, we start by replacing $M(\theta,\phi)$ with an approximate model $G(\theta,\phi)$ and comparing the result of the convolution integral $H(\theta',\phi')$ with the actual data field, $D(\theta',\phi')$, as observed from orbit. We must also replace the integration over the surface with a summation over $\Delta\theta \times \Delta\phi = 2^\circ \times 2^\circ$ (or $5^\circ \times 5^\circ$) pixels (≡ unit area). Thus Eq. (2) becomes:

$$H(\theta',\phi') = \sum_{\theta}\sum_{\phi} R(\cos\varepsilon)\cdot G(\theta,\phi)\cdot\cos\theta\Delta\theta\Delta\phi \qquad (3)$$

If G is chosen well, H should closely resemble D. The quantity:

$$\Delta(\theta',\phi') = [H(\theta',\phi') - D(\theta',\phi')] / \sigma(\theta',\phi') \qquad (4)$$

(the difference between the convolution integral and the data, divided by the a priori standard deviation σ) provides a normalized measure of the similarity. Variation outside of statistical deviation may be interpreted in terms of deficiencies in the model G. Thus the model is improved, H is recomputed, and the comparison between H and D is repeated. This iteration leads to models $G(\theta,\phi)$ which are close to $M(\theta,\phi)$. (See Appendix A for more details on the deconvolution process.)

C. Processing the Gamma Ray Spectra[4]

Once the signals are deconvolved, the spectra are stored in a large database where they can be retrieved for a particular region and/or time period. After they are adjusted to a common energy-to-channel scale (a shift based on a pre-flight calibration of line location versus temperatures of Odyssey's components), the spectra are summed to increase the statistical precision of the data. The regions of interest are either $5^\circ \times 5^\circ$ or $2^\circ \times 2^\circ$ bins in a cylindrical grid, so the spectra are collected from the deconvolved bins of whatever the desired size. Although these regions get smaller in area as the satellite gets closer to the poles, they contain approximately the same number of spectra because Odyssey passes over the near-polar bins more frequently.

Next, the intensities of the gamma rays are determined from the areas of the peaks in each spectrum that is made by summing the spectra accumulated over each grid bin. The net area is the sum of the counts above the continuum formed by scattered gamma rays. For gamma rays produced by neutron interactions, a correction is made to the peaks to normalize them to the relative cosmic ray flux. This time variant flux is determined by counting events that deposit greater than 10 MeV of energy in the GSH.

Additionally, a background correction must be made. The background signal is determined from spectra taken over the poles, where CO_2 frost is thick enough to attenuate nearly the planet's entire signal. The correction is nearly constant over all of Mars, and the data are used to correct relevant peak areas before they are used for analysis.

D. Comparing the Count Data with a Model[4]

To increase the accuracy of the maps, a model of the gamma ray flux at the satellite is calculated and compared with the data. (See Appendix B for details on the flux model.) When the recorded spectra are summed together to generate a single spectrum for a given bin, the expected counts from the model-generated spectra are also summed. The model abundance is then adjusted by the ratio of the observed counts to the modeled counts for the gamma ray line (or lines) of that element. If an element has multiple gamma ray lines, an average of all lines weighted by the inverse square of the uncertainties is calculated. For radioactive elements (e.g. K and TH), the estimated elemental abundance is the final elemental abundance, but for elements whose gamma ray emissions are a result of neutron-induced mechanisms, further calculations must be made.

Two different methods are used to analyze neutron-induced gamma ray lines depending on whether the gamma ray is the result of fast neutron inelastic scattering or thermal neutron capture. Initial fast neutron model calculations showed a simple relationship between the Si gamma ray flux and soil composition, mostly in variations of Fe and H (both of which can have a significant effect on the fast neutron flux in a given region). It was then discovered that the correction factors for Fe and H are independent of atmospheric thickness and each other and are also nearly linear over the range of compositions in question. Since absolute cosmic ray flux varies with time and is not well known, the results were normalized to a known elemental concentration, Si, since it can be determined with good precision and varies much less than other elements. Since Si also generates gamma rays from thermal neutron capture, the values of Si determined by the 1779 keV inelastic-scatter line at different places on Mars are considered the true Si values, and the ratio of apparent Si (from neutron capture line) to true Si is proportional to the relative thermal neutron flux just beneath the surface. This ratio (determined after smoothing for every 0.5˚ × 0.5˚ cell) is used to correct the H, Cl, and Fe grid data because all four elements have neutron capture cross sections that vary nearly identically with energy. Though there is circularity in determining the amount of Si using Fe and H concentrations and then determining these elements with the amount of Si, it is very small and resolved by iteration.

E. Smoothing Binned Data and Creating Maps[4]

For a given bin, the smoothing is performed through an arithmetic mean of all the values within the smoothing radius (ie. boxcar filter) for an element. Once the bins are smoothed, the maps with 5˚×5˚ or 2˚×2˚ pixels are created. These maps are generally only made for ±~45˚ because composition is difficult to determine below the CO_2 frost. Uncertainty maps are also created as it varies from location to location (most notably where elevation changes occur).

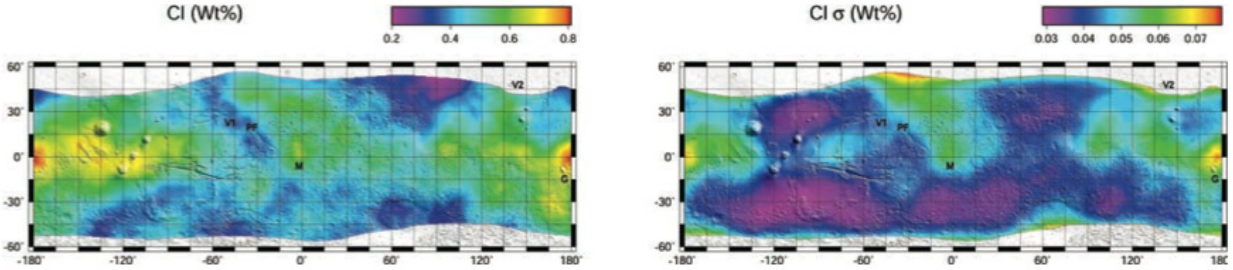

Figure 9. *A map of Cl concentrations (left) and their uncertainties (right) in low and mid latitudes of Mars.*

F. Application of the Earth Occultation and Radon Transform Method

Though sufficient for initial planetary maps, the current technique for elemental mapping suffers from its inability to effectively cope with such a large footprint. The resulting uncertainties are shown in Fig. 9 and are most significant in areas of low elevation. The method used for BATSE can more appropriately address the issue of an uncollimated detector and lead to more accurate concentration maps. For planetary mapping, our method would subtract the gamma ray background from the sky (our current signal) to read in the signal given off the planet (our current background). The difference in signal as the satellite orbited would be attributed to the surface at the limb (approximated as a straight line) that was just hidden from its field of view. We would apply the Linear Inverse Radon Transform to this data to find the source of gamma rays at a given energy and, thus, find the elemental concentration at the surface.

Though this method will theoretically work, the incredibly weak signal anywhere outside of a 1000km radius from the nadir point (<1% of the total signal)[4] will make it extremely difficult to actually record the differences being hidden by the planet's limb. A way to avoid this issue would be to implement the three-dimensional Spherical Cap Radon Transform. This method accounts for the entire spherical blockade instead of using the linear approximation of the limb. This more accurate technique could greatly enhance the spatial resolution of elemental planetary maps and greatly minimize uncertainties.

V. Conclusion/Future Work

Over the course of my internship, I have not only continued the group's project of mapping the gamma ray sky but have also expanded it to new areas of gamma ray research. The project, however, is far from completion. For the sky mapping, the next step is to create the PSF's, calculate source intensities, and use cleaning processes on each of

the 139 known source images. These cleaned images will indicate our method's accuracy in source location. Using Thomas and my code as a base, the group should be able to easily accomplish this. Once all of the known sources are located to a given accuracy, the group will then use our programs to image the entire gamma ray sky (depicted in Fig. 10). For the planetary elemental mapping, the next step is to decide on an imaging method, create a fake data set, and then compare our method's ability to reproduce it with the current method. If our technique proves to be more accurate, the group will need to acquire the Mars Odyssey and Lunar Prospector data sets and begin imaging. Once they know the relative gamma ray intensities from each point on the planet (or moon), they can normalize these counts to some known elemental concentration and produce a map of the planet.

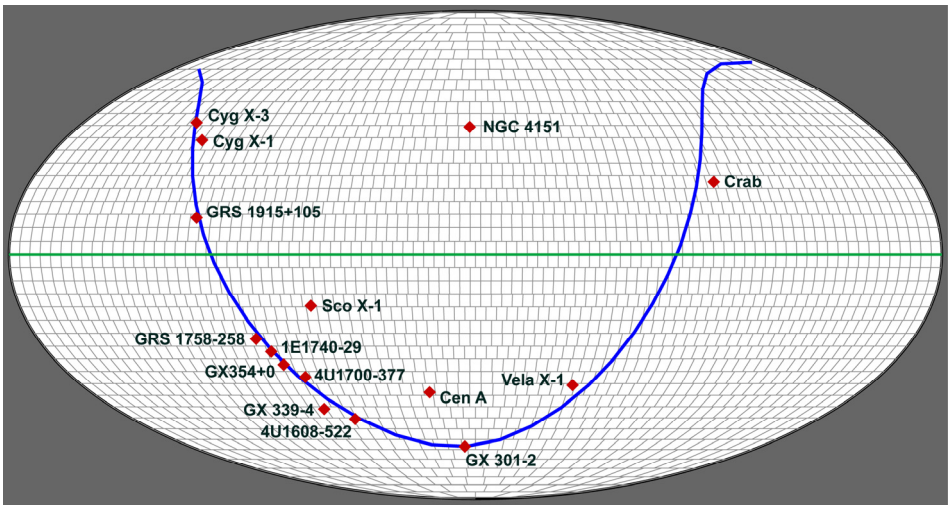

Figure 10. *The sky divided into 2584 regions of approximately 16˚×16˚ each. The blue line marks the Galactic plane and the red diamonds mark the positions of some of the 139 sources in the current EBOP catalog. Images will eventually be produced for each of the 2584 regions and summed over the 9-year BATSE mission.*

Appendix A
Deconvolution[14]

A1. Constructing the Model:

The method for shaping the model is comprised of six geometric constructs, each of which defines or modifies a feature or boundary of the elemental distribution on the planetary surface:

1) The "flat" construct gives every pixel in the model field a unit value.
2) The "border" construct places a great-circle arc through the model field. All pixels whose centers are on one side of the border are given unit value and those on the other zero value.
3) The "circle" construct assigns unit value to all pixels whose centers reside inside a circle, the center coordinates and radius of which are defined.
4) The "point" construct assigns unit value to only one identified pixel.
5) The "blob" construct assigns unit value to all pixels included in an irregular shape defined by a series of latitude and longitude descriptions.
6) The "soft" construct diffuses and field created by another construct, softening borders and peaks, by convolving that unit model field with a circular normal distribution.

Each j[th] component of the model, $g_j(\theta,\phi)$, a unit field created by a construct, is separately convolved with the response function R, and the convolved component, $C_j(\theta,\phi)$, is stored for least squares analysis.

A2. Comparing the Convolved Model with the Data:

We want to use the method of least squares to compare the convolved model H with the data D in order to improve the model G. The scalar quantity:

$$U = \sum_{\theta'} \sum_{\phi'} \Delta^2(\theta', \phi') \qquad \text{(A1)}$$

is minimized by varying the spatial and/or concentration parameters of the model G. Since G is described as a sum of the products of individual surface constructs with unit value and their respective elemental concentrations, X_j, we can write G as:

$$G(\theta, \phi) = \sum_j X_j g_j(\theta, \phi) \qquad \text{(A2)}$$

Therefore, we can rewrite Eq. (3) with Eq. (A2) as:

$$H(\theta', \phi') = \sum_{\theta} \sum_{\phi} R(\cos\varepsilon) \sum_j X_j g_j(\theta, \phi) \cdot \cos\theta \Delta\theta \Delta\phi$$

$$H(\theta', \phi') = \sum_j X_j \sum_{\theta} \sum_{\phi} R(\cos\varepsilon) \cdot g_j(\theta, \phi) \cos\theta \Delta\theta \Delta\phi$$

$$H(\theta', \phi') = \sum_j X_j C_j(\theta', \phi') \qquad \text{(A3)}$$

where $C_j(\theta', \phi')$ is the convolved unit surface produced by the j[th] construct. This separation of concentration parameters X, which is a vector comprised of linear parameters, from the nonlinear geometric parameters in g, allows us to determine X by inversion of the normal least-squares equations:

$$(C^T W C) X = C^T W D$$

$$X = (C^T W C)^{-1} C^T W D \qquad \text{(A4)}$$

where W is the diagonal weight matrix defined as $[W]_{jj} = \sigma_j^{-2}$.

A3. Procedure

1) Construct a plausible geometric model based on variations in data field
2) Treat convolved components with the least squares method to provide the best estimates of model concentrations X based on the model
3) Compute U with Eq. (A1)

   If G is a good estimate of the actual surface distribution, then U belongs to the χ^2 distribution with $\nu = N - O$ degrees of freedom, where N is the number of pixels in D and O is the number of free parameters in the model G, i.e., the number of constructs used. Use U and ν to provide a measure of the adequacy of G to describe $M(\theta, \phi)$. $\sqrt{\frac{U}{\nu}}$, called the RMS, is a useful measure of the goodness of the fit. If the a priori statistics have been correctly calculated and the model is adequate, the RMS is close to 1.
4) Until the model is refined adequately, two other displays are useful:
   - The 2-D residual field, $\Delta(\theta', \phi')$, rounded to the nearest integer – This represents a point-by-point fit of the convolved model, H, to the data, D, in units of standard deviation. Regions dominated by positive or negative residuals demonstrate deficiencies in the geometric model.
   - The distribution of normalized residuals – If H is close to D, and ν is greater than about 20, the residuals will be normally distributed with the mean equal to zero and a standard deviation of one if the a priori statistics are correct. A χ^2 test of the normal hypothesis is a very sensitive test of the least-squares assumptions once U has been minimized. Any skewness of the distribution of residuals points to problems in the model, or to spurious effects in the data.
5) Based on the RMS, the residual field, and the distribution of residuals, the geometric model is improved; the improved constructs are convolved again and the least-squares analysis repeated until the RMS can be made no smaller.

6) In practice, other considerations such as reasonableness of elemental concentrations and locations of known features are used to constrain the final selection of models.

A4. Uncertainties

The covariance matrix:

$$\sum_X^O = (C^T W C)^{-1} \qquad \text{(A5)}$$

describes the uncertainties and correlations among the concentrations without regard to the effects of variations in area and location. The effects of variation in area and location may be included in the covariance matrix by combining sensitivity of the concentrations to area and location, S, the estimated covariance matrix for the areas and locations, $\sum_p$ according to Bierman (1997).

$$\sum_X = \sum_X^O + S \sum_p S^T \qquad \text{(A6)}$$

The computation and derivation are included in the appendix of *Haines et al.* [1978].

Appendix B
Calculating the Gamma Ray Flux Model[4]

B1. Predict surface flux of gamma rays

In order to create a model for the recorded gamma ray flux, one must first predict the flux of gamma rays being produced at the surface of the planet. There are two models for this: one for gamma rays produced by radioactive elements and one for gamma rays produced by neutron interactions. For the radioactive elements, the surface emission rate can be calculated from knowledge of three components: the assumed model abundance, the known disintegration rate for gamma rays, and the attenuation of gamma rays from generation depth (using the mass attenuation coefficients from *M. J. Berger et al.* for typical Mars surface composition).[1] To successfully use these components, one must assume all elements are homogenous in the regolith.

For elements whose gamma rays are generated by neutron interactions, the model is slightly more involved. To calculate the surface emission rate, one must know the flux of incident cosmic rays, the composition of the regolith, and the thickness and composition of the atmosphere. The production of neutrons is then modeled with the Monte Carlo N-Particle eXtended (MCNPX) code for the incoming flux of cosmic rays interacting with the atmosphere and surface. The output of the MCNPX calculation is the neutron flux as a function of energy and depth and is used with the appropriate elemental cross sections to calculate a table of gamma ray fluxes as a function of the cosine of the emission angle and the atmospheric thickness. The cosine of the emission angle is important for calculating the attenuation of gamma rays produced beneath the surface, and the atmospheric thickness is important for knowing the generation and moderation of neutrons. The atmosphere's influence on the gamma ray attenuation will be factored in later.

B2. Generating counts at spacecraft

Once a model for the surface gamma ray flux is created, it must be adjusted based on orbital geometry and atmospheric attenuation. The attenuation is calculated from the atmospheric thickness based on the Mars General Circulation Model in *Haberle et al.* [1999] and is taken for the appropriate sol and approximate local time of the spectra collection. Then, the estimated gamma ray flux at the spacecraft is converted into counts based on the pre-launch measurements of efficiency as a function of angle and energy.

Acknowledgments

I thank my mentors, Dr. Martin Lo and Dr. James Ling, for their continual support and guidance during my 15-week internship. Dr. Gary Case of LSU and Thomas Shimizu were also a great help for much of my imaging work. Lastly, I thank the Jet Propulsion Laboratory and the NASA USRP program for giving me the opportunity to have this experience.

References

[1]Berger, M. J., et al. (1990), "XCOM: Photon cross sections database," [online database], http://physics.nist.gov/PhysRefData/Xcom/Text/XCOM.html.

[2]Binder, A. B. (1998), "Lunar Prospector: Overview," *Science, 281,* pp. 1475-1476.

[3]Boynton, W. V., et al. (2004), "The Mars Odyssey Gamma-Ray Spectrometer Instrument Suite," *Space Science Revews, 110*, pp. 37-83.

[4]Boynton, W. V., et al. (2007), "Concentration of H, Si, Cl, K, Fe, and Th in the low- and mid-latitude regions of Mars," *J. Geophys. Res., 112*, E12S99, doi:10.1029/2007JE002887.

[5]El Maarry, M. R. and O. Gasnault (2009), "A preliminary assessment of the role of impact craters in forming hydrous minerals on the surface of Mars," *Annual Lunar and Planetary Science Conference*, League City, Texas.

[6]Evans, L. G., R. C. Reedy, R. D. Starr, K. E. Kerry, and W. V. Boynton (2006), "Analysis of gamma ray spectra measured by Mars Odyssey," *J. Geophys. Res., 111*, E03S04, doi:10.1029/2005JE002657 [printed 112(E3), 2007].

[7]Feldman, W. C., B. L. Barraclough, K. R. Fuller, D. J. Lawrence, S. Maurice, M. C. Miller, T. H. Prettyman, and A. B. Binder (1999), "The Lunar Prospector gamma-ray and neutron spectrometers," *Nuclear Instruments and Methods in Physics Research, A 422*, pp. 562-566.

[8]Feldman, W. C., et al. (2004), "Gamma-Ray, Neutron, and Alpha-Particle Spectrometers for the Lunar Prospector mission," *J. Geophys. Res., 109*, E07S06, doi:10.1029/2003JE002207.

[9]Fishman, G. J., et al. (1989), *in Proc. Gamma Ray Observatory Science Workshop*, ed. W. Johnson (Greenbelt: GSFC), 2.

[10]Gindikin, S. G. (1992), "Some Notes on the Radon Transform and Integral Geometry," *Mh. Math., 113*, pp. 23-32.

[11]Haberle, R. M., et al. (1999), "General circulation model simulations of the Mars Pathfinder atmospheric structure investigation/meteorology data," *J. Geophys. Res., 104*, pp. 8957-8974.

[12]Hahn, B. C., et al. (2007), "Mars Odyssey Gamma Ray Spectrometer elemental abundances and apparent relative surface age: Implications for Martian crustal evolution," *J. Geophys. Res., 112*, E03S11, doi:10.1029/2006JE002821.

[13]Haines, E. L. and A. E. Metzger (1978), "High Resolution Thorium Maps by Means of Spatial Deconvolution as Applied to the Aristarchus Plateau," *Annual Lunar and Planetary Science Conference*, League City, Texas, pp. 445-447.

[14]Haines, E. L., M. I. Etchegaray-Ramirez, and A. E. Metzger (1978), "Thorium concentrations in the lunar surface. II: Deconvolution modeling and its application to the regions of Aristarchus and Mare Smythii," *Proc. Lunar Planetary Sci. Conf.*, pp. 2985-3013.

[15]Helgason, Sigurdur, *Radon Transform*, 2nd ed., Birkhäuser, Boston, 1999, pp. 1-169.

[16]Keller, J. M., et al. (2003), "Preliminary Correlations of Mars GRS Elemental Abundances with Thermal Inertia, Albedo, and Rock Abundance," *Annual Lunar and Planetary Science Conference*, League City, Texas.

[17]Lawrence, D. J., W. C. Feldman, B. L. Barraclough, A. B. Binder, R. C. Elphic, S. Maurice, and D. R. Thomsen (1998), "Global Elemental Maps of the Moon: The Lunar Prospector Gamma-Ray Spectrometer," *Science, 281*, pp. 1484-1489.

[18]Lawrence, D. J., R. C. Elphic, W. C. Feldman, O. Gasnault, I. Genetay, S. Maurice, and T. H. Prettyman (2002), "Small-Area Thorium Enhancements on the Lunar Surface," *Annual Lunar and Planetary Science Conference*, League City, Texas.

[19]Ling, J. C., et al. (1997), "Gamma-Ray Spectra and Variability of Cygnus X-1 Observed by BATSE," *Ap. J. 484, 375*.

[20]Ling, J. C., et al. 2000, "A BATSE Earth-Occultation Catalog of 0.03-1.8 MeV Gamma-Ray Source Spectra and Light Curves for Phases 1-3 (1991-1994)," *ApJS, 127,* pp. 79-124.

[21]Ling, J. C. and Wm. A. Wheaton (2003a), "Gamma-Ray Spectra and Variability of the Crab Nebula Emission Observed by BATSE," *Ap. J. 598, 334*.

[22]Ling, J. C. and Wm. A. Wheaton (2003b), "BATSE Soft γ-Ray Observations of GROJ0422+32," *Ap. J., 584*, 399.

[23]Ling, J. C. and Wm. A. Wheaton (2005), "Gamma-Ray Spectral State Transitions of GROJ1719-24," *Ap. J, 622, 492*.

[24]Ling, J. C., et al. (2009), "BATSE Soft Gamma Rays Tomographic Sky Imaging with Radon Transforms," *Bulletin of the American Astronomical Society, 41*, p.671.

[25]Masarik, J. and R. C. Reedy (1996), "Gamma ray production and transport in Mars," *J. Geophys. Res., 101,* pp. 18, 891-18,912.

[26]Prettyman, T. H., R. C. Elphic, W. C. Feldman, J. R. Murphy, S. Nelli, T. N. Titus, and R. L. Tokar (2005), "Spatial Deconvolution of Mars Odyssey Neutron Spectroscopy Data: Analysis of Mars Southern Seasonal Cap," *Annual Lunar and Planetary Science Conference*, League City, Texas.

[27]Prettyman, T. H., J. J. Hagerty, R. C. Elphic, W. C. Feldman, D. J. Lawrence, G. W. McKinney, and D. T. Vaniman (2006), "Elemental composition of the lunar surface: Analysis of gamma ray spectroscopy data from Lunar Prospector," *J. Geophys. Res., 111*, E12007, doi:10.1029/2005JE002656.

[28]Reedy, R. C. and J. R. Arnold (1973), "Expected Gamma Ray Emission Spectra from the Lunar Surface as a Function of Chemical Composition," *J. Geophys. Res., 78,* pp. 5847-5866.

[29]Reedy, R. C. (1978), "Planetary Gamma Ray Spectroscopy," *Proc. Lunar Planetary Sci. Conf.*, pp. 2961-2984.

[30]Shaw, S. E., et al. (2004), "Gamma-ray all-sky imaging with the Burst and Transient Source Experiment," *A&A, 418,* pp.1187-1200.

[31]Starck, Jean-Luc and Murtagh, Fionn, *Astronomical Image and Data Analysis*, 2nd ed., Springer-Verlag, Berlin, 2006, pp. 71-110.